Real-Time Teleoperation of Magnetic Force-Driven Microrobots With 3D Haptic Force Feedback for Micro-Navigation and Micro-Transportation

Jaeyeon Lee, Xiao Zhang, Chung Hyuk Park, and Min Jun Kim

***Abstract*—Untethered mobile microrobots controlled by an external magnetic gradient field can be employed as advanced biomedical applications inside the human body such as cell therapy, micromanipulation, and noninvasive surgery. Haptic technology and telecommunication, on the other hand, can extend the potentials of untethered microrobot applications. In those applications, users can communicate with the robot operating system remotely to manipulate microrobots with haptic feedback. Haptic sensations artificially constructed by the wirelessly communicated information can assist human operators to experience forces while controlling the microrobots. The proposed system is composed of a haptic device and a magnetic tweezer system, both of which are integrated through a teleoperation technique based on network communication. Users can control the microrobots remotely and feel the haptic interactions with the remote environment in real-time. The 3D haptic environment is reconstructed dynamically by a model-free haptic rendering algorithm using a 2D planar image input of the microscope. The interaction between microrobots and environmental objects is haptically rendered as 3D objects to achieve spatial haptic operation with obstacle avoidance. Moreover, path generation and path guidance forces provide virtual interaction for human users to manipulate the microrobot by following the near-optimal path in path-following tasks. The potential applications of the presented system are medical remote treatment in different sites, remote drug delivery by avoiding physically penetrating through the skin, remotely-controlled cell manipulations, and biopsy without a biopsy needle.**

***Index Terms*—Automation at micro-nano scales, haptics and haptic interfaces, medical robots and systems, micro/nano robots, telerobotics and teleoperation.**

I. Introduction

MICROROBOT applications in both *in vitro* and *in vivo* environments have been interesting topics in the biomedical research field since they have the potential to revolutionize the healthcare industry. When microrobots are combined with wirless control techniques, applications like *in situ* sensing, cell therapy, micromanipulation [1]–[4], and targeted/localized drug delivery [5]–[7] can be achieved to transform the processes of minimally invasive surgery, drug delivery, and biopsy procedures. Wireless control within such a small scale is limited to optical, electrical, and magnetic techniques, which have been deployed in many applications such as electromagnetic coil systems, photonic force microscopy, optical tweezer systems, and magnetic tweezer systems [8]–[12].

An optical tweezer system generates optical forces with a highly focused laser beam. However, the control resolution is typically poor and the system is highly power-consuming. Additionally, tissues surrounding the controlled object will be affected by the laser beam if they share a similar refraction index and thus ruining further operations [11], [13]. An electromagnetic coil system, in contrast, generates a rotating magnetic field to produce a magnetic torque on microrobots [1], [8], [14], [15]. The movement resulting from magnetic torques has two general characteristics on the microrobot: chirality (helical microrobot, etc.) and flexibility (such as sperm-like microrobot) [16], [17]. However, when concentrating on a small workspace, transforming power into a rotating magnetic field to achieve microrobotic movements has a low efficiency compared to a magnetic tweezer system, since the magnetic manipulation performance is highly dependent on the shape, rigidity, and magnetism of the microrobots. The mechanism of the magnetic tweezer system presented in this study can be idealized as generating a magnetic gradient field to produce a magnetic force on microrobots [1], [18]–[21]. When the system is activated, the magnetic gradient field surrounds the sharp tip of magnetic poles and then spreads over the working space, where it interacts with magnetic microrobots to produce a magnetic force. Since the strength of the gradient field decreases significantly as the distance increases from the pole tip, high power output is necessary for maintaining a large workspace [1], [22]–[24]. While most of the magnetic tweezer systems developed by other research groups have relatively small workspaces and limited power, ours has a superior performance as discussed in our previous work [1]. Currently, most microrobot systems concentrate on the control performance of the microrobot while the human interaction aspect is not well investigated, which is essential in biomedical applications as medical professionals or researchers play a vital role in the operations [25]. It is important to build up

Manuscript received October 13, 2020; accepted February 8, 2021. Date of publication February 19, 2021; date of current version March 8, 2021. This letter was recommended for publication by Associate Editor L. Zhang and Editor X. Liu upon evaluation of the reviewers' comments. This work was supported by the National Science Foundation (CMMI #1712096) (Kim) and in part by the GW Startup grant (Park). *(Jaeyeon Lee and Xiao Zhang contributed equally to this work.) (Corresponding authors: Chung Hyuk Park; Min Jun Kim.)*

Jaeyeon Lee and Chung Hyuk Park are with the Department of Biomedical Engineering, George Washington University, Washington, DC 22031 USA (e-mail: jaeyeon.lee2902@gmail.com; chpark@gwu.edu).

Xiao Zhang and Min Jun Kim are with the Department of Mechanical Engineering, Southern Methodist University, Dallas, TX 75251 USA (e-mail: xiaozhang@smu.edu; mjkim@lyle.smu.edu).

This letter has supplementary downloadable material available at https://doi.org/10.1109/LRA.2021.3060708, provided by the authors.

Digital Object Identifier 10.1109/LRA.2021.3060708

the interaction between control systems and human operators so that one can give guidance to the operation when either one is confronted with problematic scenario.

Haptic force feedback techniques have been verified to be a significant tool to achieve teleoperation of robotic systems [25], [26]. Advantages of the haptic system have been confirmed in cardiothoracic procedures [27], microneedle positioning [28], telerobotic catheter insertion [29], palpation [25], cell injection [30], [31], and even micro-manipulation [32]–[35]. Multiple haptic feedback devices have also been developed so far to control and manipulate microrobot systems. Haptic sensations from interaction between a self-folding soft magnetic gripper and its environment were investigated in [34], where the human operator intuitively controlled a magnetic gripper using a haptic interface. In terms of visual sensing by the haptic device, Pacchierotti *et al.* [33] employed a haptic interface for a user to remotely control self-propelled microrobots to target a goal with particle-filter visual sensing that visually tracks the position of the microrobots. Asgari *et al.* [36] provided a haptic force generation method for a microrobotic cell injection procedure. A 3D particle-based model was proposed to simulate the deformation of the cell membrane and corresponding cellular forces. Faroque *et al.* [37] proposed a large-scale virtual reality training system with a haptic device, in which virtual fixtures and force feedback was generated for the microrobotic cell injection procedure, to guide user for virtual micropipette operations by force feedback. So far, the usability and reliability of haptic interaction with the microrobot system have been significantly advanced for potential human operators. However, most of the existing techniques provide haptic force feedback through either an ambient interaction or direct contact force. Moreover, onsite interactions have been typically prioritized, while remote operations over large distances have not been conducted enough, despite the fact that remote control of the microrobot applications with haptic interactions is crucial to extending the utility of remote therapy and surgery.

In this letter, we present a microrobot control framework using haptic interaction based on the networked teleoperation between a magnetic tweezer system and a haptic interface. Haptic guidance force for near-optimal path following and haptic force feedback for real-time interactions with the environments are implemented in teleoperation settings over two facilities more than 2000km apart. An attractive force is utilized to achieve haptic guidance for path following and obstacle avoidance, while a repulsive force based on the potential field and virtual-proxy force was implemented to produce the haptic interaction that allowed users to feel the virtual environments. We provide the haptic interaction forces of both ambient and contact interactions to improve usability. The proposed system includes an image-based 3D haptic rendering algorithm, which reconstructs artificial 3D objects by reflecting dynamic shape changes of the planer objects for practical haptic interaction. The 2D image was transmitted remotely (real-time transmission between George Washington University in Washington, D.C. and Southern Methodist University in Dallas, Texas, approx. 2138 km apart) from a magnetic tweezer system, with multiple arbitrarily shaped objects within the field-of-view, to create real-time haptic force feedback and enable the manipulation of microrobots. The notable contributions of our work described in this letter are as follows.

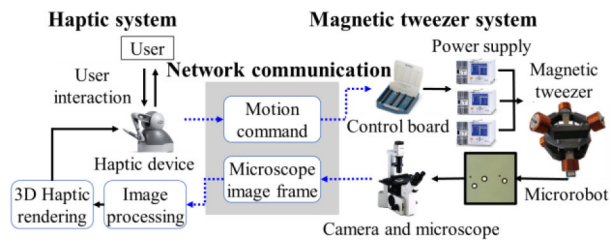

Fig. 1. Microrobot haptic interaction system. Left part is a haptic interface and right part is a magnetic tweezer system. Data flow of image frames and control commands are shown as arrow directions.

1) Haptic interactions for near-optimal path following, object contact interaction with proxy-force, and object ambient interaction with an artificial potential field are implemented to assist microrobot controls.
2) Dynamic path planning is applied based on the user's intended haptic operation, in which the effective path with obstacle avoidance is dynamically generated and updated.
3) 3D object reconstruction is accomplished by reflecting dynamic shape changes of the objects in a 2D planar image using the model-free haptic rendering.
4) A closed-loop teleoperation system is achieved with a wireless communication between the magnetic tweezer system and the haptic interface system.
5) The practical system is implemented and tested with a commercial haptic device in macroscale and magnetic tweezer in microscale under practical distance data communications.

The rest of the letter is organized as follows. Section II gives descriptions of the overall microrobot haptic feedback system. Details of the magnetic tweezer system, teleoperation implementation, and haptic feedback are followed in Sections III and IV, respectively. Section V represents the dynamic path planning algorithm and Section VI shows our experimental results to validate the proposed system. The conclusion is provided in Section VII.

II. Microrobot Haptic Interaction System

A. Illustration of Haptic and Magnetic Tweezer System

The integration of a magnetic tweezer system with a haptic interface is illustrated in Fig. 1, where the two systems communicate with a TCP/IP network communication protocol. The haptic interface generates haptic feedback force based on the motion of microrobots and environmental objects, which is received from the magnetic tweezer system; the control command is then sent back to microrobots for navigation. Haptic rendering, image processing, path planning, and network communication were developed in C++, while the magnetic tweezer control, microscopic image processing, and network communication were established in MATLAB.

The haptic interface (Geomagic touch haptic device, 3D Systems, Rock Hill, SC) is operated by a 6-DOF (degree of freedom) pen-type stylus gripper, which is serially connected to the haptic device body. The device can measure the 6-DOF position and orientation of the user's operation and generate 3-DOF force feedback in x, y, and z directions. The haptic control software is developed using the open-source haptic library CHAI3D to

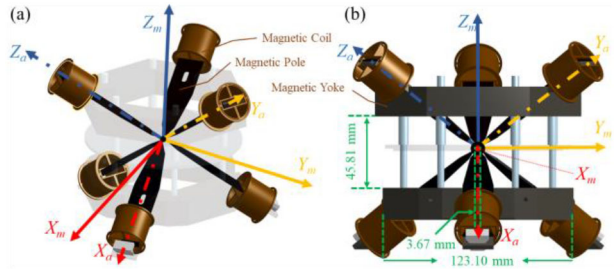

Fig. 2. Our magnetic tweezer system and its schematics. (a) Transparent view and (b) front view of a magnetic tweezer with illustrations of the actuation and measurement coordinate systems.

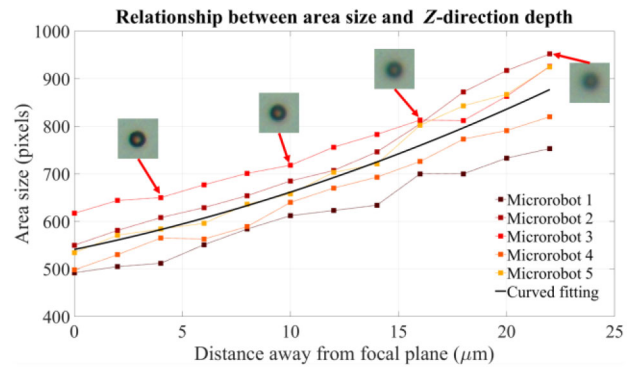

Fig. 3. Relationships between visually tracked sizes of microrobots (area size) and the actual z-depth.

ensure the compatibility over the multiple operating systems and diverse haptic device platforms. As shown in Fig. 2, the magnetic tweezer system consists of six magnetic poles on a double-layer structure with three poles on top and bottom planes, each pole has a magnetic coil of 527 turns, which is made of AWG-25 heavy-built insulation coating copper wire, attached to the end. Additionally, the magnetic yoke is 3D printed with magnetic material that guarantees durability and rigidity, as well as improving magnetic gradient field generation efficiency. Cobalt iron alloy (VACOFLUX 50, VACUUMSCHMELZE GmbH & Co.KG) was selected for magnetic poles due to its high saturation (2.35 T) feature and machinability of the sharp-tipped shape. A sharp tip is necessary to produce a strong magnetic gradient field to achieve the $2\times2\times0.5$ mm^3 wide effective workspace so that a large swarm of microrobots can be controlled. Six magnetic poles are configured in a manner to form an inclined Cartesian coordinate system (actuation coordinate system). Coordinates in the measurement coordinate system can be obtained by the coordinate system rotation. The preset angles between X_a-X_m, Y_a-Y_m, and Z_a-Z_m are 35.26°, 45°, and 54.74°, respectively. The transformation from the measurement coordinate system to the actuation coordinate system is shown in (1-2) [1], [2], [8]:

$$\begin{aligned} {}^{\boldsymbol{a}}_{\boldsymbol{m}}\boldsymbol{R} &= [\boldsymbol{R_x}\,(45^\circ)]\,[\boldsymbol{R_y}\,(35.26^\circ)] \\ &= \begin{bmatrix} 0.8165 & 0 & -0.5774 \\ 0.4082 & 0.7071 & 0.5774 \\ 0.4082 & -0.7071 & 0.5774 \end{bmatrix}, \end{aligned} \tag{1}$$

$$\boldsymbol{X_a} = \begin{bmatrix} x_a \\ y_a \\ z_a \end{bmatrix} = {}^{\boldsymbol{a}}_{\boldsymbol{m}}\boldsymbol{R} \cdot \begin{bmatrix} x_m \\ y_m \\ z_m \end{bmatrix} = {}^{\boldsymbol{a}}_{\boldsymbol{m}}\boldsymbol{R} \cdot \boldsymbol{X_m} \tag{2}$$

B. 3D Position Computation

A microrobot can be controlled in 3D space, however, only the 2D planar position (x-y plane) of microrobot can be collected directly. In our previous work [8], the visually tracked area sizes of microrobots were utilized to achieve 3D tracking and control [38], [39], and the relationship to z-depth is shown in Fig. 3, which was obtained from five microrobots (same type). All microrobots were sedimented on the glass slide. To simulate microrobot's precise motion along z direction, we utilized the z-depth knob control on the microscope (1 μm per increment) to create relative movement between microscope lens and sample platform, the environmental factors such as illumination, fluid type and camera expourse were kept constant to ensure uniformity for all experiments. All experiments began with microrobots staying on the bottom of the sample chamber, so its z-depth is initiated as zero with a microscope focusing on it. As time goes on, the area size of microrobots will increase as they are navigated upwards. Note that environmental objects are assumed stationary on the bottom since they are not affected by the magnetic force. The area size of each microrobot in the image is analyzed and compared with the initial value to update the z-depth through the quadratic relationship in (3). Thus, the displacement Δz can be calculated as:

$$\begin{aligned} &S = az^2 + bz + c, \\ &S_{up} - S_{init} = a\,(z_{up} - z_{init})\,(z_{up} + z_{init}) + b\,(z_{up} - z_{init})\,. \end{aligned} \tag{3}$$

The area sizes (S) of both S_{up} and S_{init} conditions are determined from the experiments. The coefficients a and b are curve-fitting results of the relationship in Fig. 3 with corresponding values of 0.2684 and 9.3746, and c is neglected as it will be canceled out. The bottom of the experimental chamber is set as the initial plane with $z_{init} = 0$, and z_{up} can then be calculated by solving the quadratic function as:

$$\begin{aligned} &S_{up} - S_{init} = az_{up}^2 + bz_{up}, \\ &z_{up} = \frac{-b + \sqrt{b^2 + 4a\,(S_{up} - S_{init})}}{2a}. \end{aligned} \tag{4}$$

III. Teleoperation Controls

A. Teleoperation Scheme

The haptic-microrobot teleoperation system was designed by an impedance control scheme with a position-based force rendering. The impedance control measures the motion of the haptic device to manipulate the force of the magnetic tweezer. It has relatively low inertia and is highly back-drivable compared to admittance control. The equation of motion of the microrobot in 3D space can be derived as:

$$m\ddot{\vec{x}} - \vec{f_d} = \vec{f_m} \tag{5}$$

where m is the mass of the microrobot, and $\vec{f_d}$ and $\vec{f_m}$ are drag and magnetic forces, respectively. Since the forces applied to

the microrobot are determined by the displacement of the haptic interface, the magnitude of the magnetic force $\vec{f}_m$ is controlled by the haptic interface and can be expressed by the haptic interface displacement such that $\vec{f}_m = K\vec{x}_h$, where $\vec{x}_h$ is the haptic device displacement in 3D. $K = 1$is the scaling constant to map the magnetic tweezer workspace to the haptic interface workspace. Gravity was negligible as a high concentration NaCl solution (20% w/v) was used to prevent sedimentation. Adhesive force is included in the drag force term ($\vec{f}_d$) of the NaCl solution, and friction is negligible because the microrobots are moving above the glass slide.

Reliable operations for the teleoperation environments can be assumed since the communication was fast enough for the microrobots' operation via the haptic device (average time delay = 45.47 ms/frame with SD = 27.02 ms/frame for transmitting series of 512×512 color images). The microrobots were operated at a micro-scaled workspace with relatively slow speed (approx. 2∼3 $\mu m/s$ with maximum magnetic force) compared to the haptic operation. Therefore, we can guarantee the *in-situ* perception of the haptic feedback for navigation and transportation of the microrobots wirelessly by referring the fact that f_m is zero when x_h is zero, so that the drag force f_d in (5) will dissipate the energy completely. The acceleration term in (5) will be negligible due to the extremely small mass, and very slow and steady speed of the microrobots, which will cause the acceleration to be practically zero. On top of that, a viscosity force feedback was implemented to the haptic device to reduce the instability and limit the control input speed of the haptic operation by preventing abrupt motions of the haptic user.

B. Network Communication

Sufficient speed and reliability of the data communication are important for the stable operation of a bilateral haptic-microrobot interaction system. The network communication scheme of our proposed system is displayed in Fig. 1 with blue dot lines. The raw color image data from the magnetic tweezer was encoded into JPEG format to compress the data size dramatically while minimizing the compression time. The communication data packet from the magnetic tweezer system to the haptic interface side was designed with three sub-components—header, body, and end bits—to ensure the correct reception of data in real-time. Header bits contain the position of the user-selected microrobot and body bits encompass the compressed image data. Since the binary format data size of the encoded color image varies based on each image frame, the size of the binary format data is communicated prior to the binary image data in the body bits. The end bits are transmitted to notify the end of each packet. The binary format data of the color image is then decoded to rebuild the color image at the receiver side. In the opposite direction, the control command by the haptic device is transmitted to the magnetic tweezer side. The control command is composed of a 3D direction vector and a scalar for the force magnitude. To guarantee the reliability of the bidirectional communication, data packet check and confirmation protocols are applied. The communication data update rate is fixed as 10 frames/s by considering the stable communication and continuous haptic operations for intuitive control of the teleoperation system.

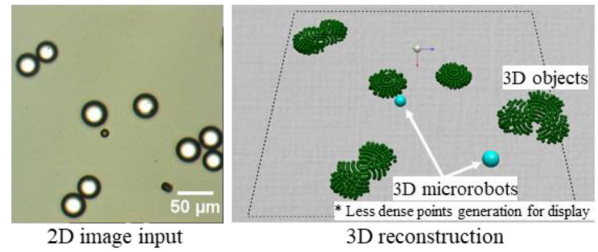

Fig. 4. 3D volume reconstruction (microrobots and environmental objects). 3D cloud points reconstruction by 2D microscope input image.

IV. Haptic Feedback Implementation

A. Object Classification and 3D Volume Reconstruction

After receiving the raw image, the haptic interface side classifies all objects by their size information obtained through image processing. The diameter of a single-bead microrobot is approximately 10.6 μm while that of the environmental objects is ranging from 27.0 to 32.0 μm. Note that a color detection by the HSV (Hue, Saturation, Value) image was deployed at haptics interface side for the swarm operation of the microrobots in Experiment 3.

As the received image is in 2D, the visually-identified objects (micro-robots and obstacles) need to be reconstructed to 3D objects for the spatial haptic rendering. Using positions and diameters of the microrobots in the 2D image, 3D volume reconstruction is processed by converting 2D circular objects to 3D spherical objects located at the same position on the *x*-*y* plane with initial *z*-depth as zero. The 3D volumized environmental objects are reconstructed using ellipsoidal 3D cloud points. Although the environmental objects used in the experiments are assumed as spheres, the ellipsoid was used as a potential extension for general applications. By adjusting the radius on the *z*-axis, the different shapes of the environmental objects can be reconstructed more effectively in the general case. Cloud points, which represent components of the surface of a 3D ellipsoid, are generated at the same position of the 2D environmental objects with a circular radius on the *x*-*y* plane. The radius of the ellipsoid on the *z*-axis is defined as a quarter of the circular radius to prevent any presence of a large empty space of the 3D reconstructed points. Part of the 3D ellipsoid points is excluded by filtering out the points that are not overlaid on the 2D object (Fig. 4). This procedure upgrades the environmental objects in the 2D image to a higher degree (3D) objects by reflecting different objects' shape, making haptic rendering in 3D space possible.

B. Artificial Potential Field Force

The haptic force feedback consists of two different forces, the ambient force near the environmental objects and the contact force. Ambient force is generated by a repulsive artificial potential field while the contact force is generated by a virtual proxy force. Users can feel the haptic feedback when the haptic probe enters the potential field of the objects. The haptic workspace is treated as a 3D grid where the 3D cloud points of environmental objects are superimposed. Each grid cell occupied by the point contributes to a repulsive potential field.

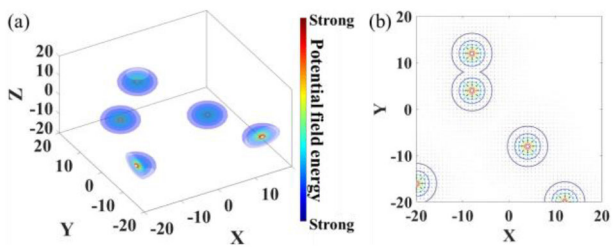

Fig. 5. Illustrations of the repulsive potential field around 3D objects. (a) 3D repulsive potential fields and (b) potential fields as seen on the x-y plane.

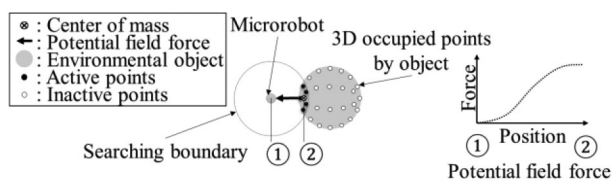

Fig. 6. Potential field force generation with active occupied points.

Fig. 5 illustrates the 3D potential fields around a single particle for the haptic motion control space. The repulsive haptic forces are designed to be centered inside the obstacle in order to prevent the haptic probe penetrating the virtual space inside of the obstacle in the mapped haptic workspace. The repulsive potential field U_{ref} can be generated by occupied cells $p_i \in G$ as:

$$U_{ref}\left(x, x_{pi}\right) = \begin{cases} \frac{1}{2}\eta\left(\frac{1}{\|x-x_{pi}\|} - \frac{1}{\rho_0}\right), & \|x - x_{pi}\| \leq \rho_0 \\ 0, & \text{otherwiase,} \end{cases} \tag{6}$$

where x is the position of the haptic probe, x_{pi} is the position of occupied cells, η is a positive scaling factor, and ρ_0 is the range of influence. The force is computed by the negative gradient of the potential field. The repulsive force F_i exerted by each cell p_i and the total repulsive potential field U of all occupied cells can be written as

$$F_i\ \left(x, x_{pi}\right) = -\nabla U_{ref}\left(x, x_{pi}\right), \tag{7}$$

$$U = \sum_{p_i \in C} U_{ref}\left(x, x_{pi}\right). \tag{8}$$

Therefore, the total repulsive force on the haptic probe by the 3D occupied cells can be calculated as

$$F = -\sum_{p_i \in C} \nabla U_{ref}\left(x, x_{pi}\right). \tag{9}$$

The center of mass of the occupied grid cells, within a searching boundary from the haptic probe, is used to compute the direction vector and magnitude for the potential field force. Fig. 6 shows the potential field force generation strategy.

C. Virtual-Proxy Force

The proxy-based haptic interaction is employed to generate a contact force from the surface of the objects that feels like a relatively stiff surface to the user. This approach, which uses a notion of the virtual proxy, is widely used in haptic interactions [40]–[42]. The force response, $\vec{f}_f$, of the haptic device in 3D using the spring-damper model that connects the virtual proxy and the haptic probe can be written as:

$$\vec{f}_f = k\left(\vec{x}_{proxy} - \vec{x}_{probe}\right) + d\left(\vec{v}_{proxy} - \vec{v}_{probe}\right), \tag{10}$$

where $\vec{x}_{probe}$ and $\vec{x}_{proxy}$ are the positions of the haptic probe and the virtual proxy in 3D while $\vec{v}_{probe}$ and $\vec{v}_{proxy}$ are the velocities of the virtual proxy and the haptic probe in 3D, respectively. The k is the stiffness constant and d is the damping constant. Empirical parameters of the $k = 280$ and $d = 2$ are selected for the best performance and user experience of the teleoperation control of the proposed system.

Forces by the potential field and virtual proxy on the 3D environmental objects are transmitted to the haptic interface side to generate the haptic feedback force when the haptic probe is approaching and touching the environmental objects. Once the haptic probe enters the potential field area, the user starts to feel the repulsive forces increasing proportionally as the haptic probe is getting into the high gradient region of the object's potential field. Moreover, when the haptic probe touches the surface of the environmental objects, the proxy force is added to produce a stiff contact force for better intuitve haptic interaction.

D. Computational Complexity Reduction Strategy

To provide seamless haptic interaction (quality of service) while enhancing the networked teleoperation performances, a computational cost reduction strategy with efficient search algorithm was applied to achieve smooth operations and intuitive usability. Any environmental objects within a certain spherical boundary from the haptic probe are explored rather than searching the full range of the workspace to detect the objects. Moreover, a region-of-interest (ROI) based local computations are employed that utilizes only part of the 3D points of the active environmental objects (active points in Fig. 6) when they are within a searching boundary from the haptic probe. Those strategies reduce the computational complexity to ensure continuous operation.

V. Dynamic Path Planning With The Haptic Operation

Dynamic path planning of the haptic-microrobot system produces an effective path adaptively in the realistic haptic environment. An instant target is created based on the dynamic movement of the haptic device so that the near-optimal path from the current haptic position to the instant target is dynamically generated by reflecting the user's intention of the haptic control. When the haptic device moves, the near-optimal path is locally generated in the *x-y* plane, and the path following force for the haptic device is activated. In the path following features, *z*-direction motion is assumed to be zero.

A. Path Planning Field Generation

A path planning workspace is modeled as a finite number of identical square cells based on the pixel coordinates of the received image. The square cells are occupied with environmental objects or empty. The repulsive force field by the environmental objects is implemented using the Gaussian filtering so that image depth of the pixel values of the Gaussian blurred image can

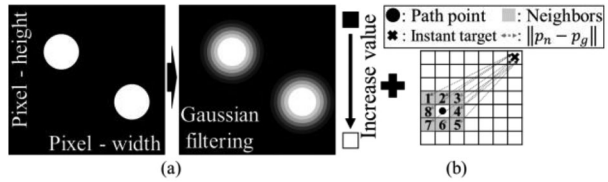

Fig. 7. Force field for the path generation. (a) Repulsive force field generated by Gaussian filtering and (b) attractive force field by the instant target.

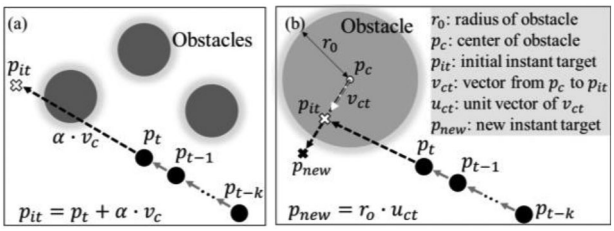

Fig. 8. Instant target creation. (a) Instant target creation strategy and (b) target creation outside of environmental object.

be treated as the magnitude of the repulsive force field. The attractive force field U_a to the instant target is defined by the distance between a neighbor cells p_n of the current path point p_c and instant goal p_g as

$$U_a = \frac{1}{2}\,\xi \cdot \|p_n - p_g\|^2,\ p_n \in N,\ neighbors\ of\ p_c, \quad (11)$$

where ξ is the magnification constant. The force field for path planning is the combination of the repulsive and attractive force fields as shown in Fig. 7.

B. Instant Target Creation

The real-time path generation reflecting the user's intentions of the haptic operation is processed by dynamically creating an instant target. We assume that the user is mostly aiming to keep the haptic movement in the direction similar to previous motions. Fig. 8 (a) represents the instant target creation. The position history of the haptic device is recorded, and differences of the position by time are averaged to estimate the future location of the haptic motion. Instant target p_{it} is a certain step $(\alpha \cdot v_c)$ forward from current haptic position p_t. Fig. 8 (b) illustrates the instant target creation outside of any environmental objects, with which the algorithm avoids the path generation directing to the collision course with the environmental objects. If an instant target is created inside of the obstacle during the instant target creation process, a new target is recreated at the closest boundary of the obstacle using the original target point (p_{it}), radius (r_0), and center position (p_c) of the related obstacle, and then replaced with the p_{it} to create the instant target outside of the obstacle as shown in Fig. 8 (b). Additionally, the instant target generation is temporarily paused when the user closely detours the environmental objects since the algorithm can create an unintended target due to the circular detouring motion of the haptic operation.

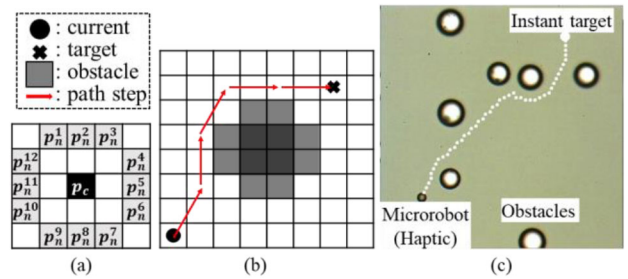

Fig. 9. Dynamic path planning of the microrobot navigation. (a) Defined neighbors, $\boldsymbol{n} = 12$. (b) Path step from the start to a target and (c) path generation example.

C. Path Planning

After creating the instant target, the path planning algorithm generates a guidance path from the current haptic position to the target while avoiding environmental objects. Each intermediate path point is selected among the neighbors of the current path point. The neighbors of the current path point are defined with 12 grid cells, with consideration of the computational cost and path smoothness, as shown in Fig. 9 (a). The path generation algorithm iteratively selects the next path point until the instant target is reached. The next path point p_f is selected by minimizing a cost as:

$$p_f = \underset{p_n \in N}{\operatorname{argmin}} \left\{ w_t \cdot U_a\left(p_n\right) + w_o \cdot U_r\left(p_n\right) \right\}, \quad (12)$$

where N is all neighbors of current path point p_c, and p_n is neighbors $(p_n^1,\ p_n^2,\ \ldots, p_n^{12})$. The cost is defined by the repulsive and attractive force fields by the environmental objects and instant target with adjustable weights. $U_a(x)$ and $U_r(x)$ are attractive and repulsive force fields, respectively. Fig. 9 (b-c) illustrates the path planning steps and path generation.

Due to the discretization of workspace in the proposed path planning, the path can be trapped in certain grids by repeatedly selecting the next path with the same sequence. The proposed algorithm processes a random selection of the next path if the path selection memory shows only repeated transits between two neighbors and does not reduce the distance to the target. Haptic force guidance to follow the effective path assists the user to operate the microrobot with the haptic feedback. In the dynamic path planning, the intermediate path point is gradually generated from the current haptic position to the target. At that time, an attractive force is applied to the haptic device to minimize the distance from the current haptic position to the intermediate path point. Eventually, the user can feel the haptic guidance force during path generation until the haptic probe reaches the target. If a new instant target is generated during the path following, then a new path planning from the current haptic position to the new target is triggered.

VI. Experiments and Results

Our experimental design and processes are described as follows. Three experiments were designed to evaluate our proposed framework: (1) microrobot manipulation with haptic feedback, (2) dynamic path planning with the path following force, and (3) micro-object transportation. In all experiments,

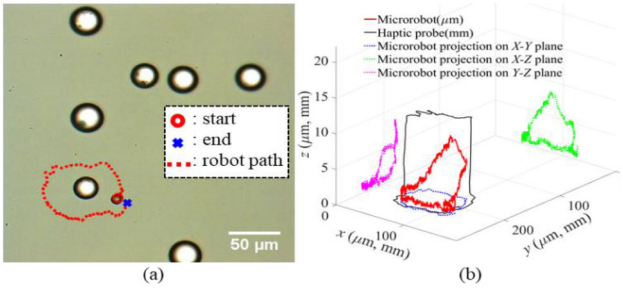

Fig. 10. Experiment 1: single microrobot manipulation with haptic feedback in 3D space. (a) Microrobot path by the haptic control for obstacle avoidance. (b) 3D motion of microrobot and haptic probe.

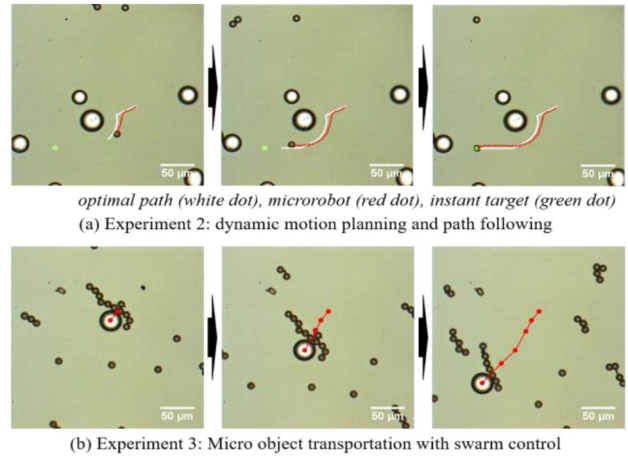

Fig. 11. Path following and swarm experiments. (a) Experiment 2: dynamic motion generation and microrobot path by the haptic control with the path following force. (b) Experiment 3: micro object transportation with swarm control of the microrobots.

a user-selected microrobot in the workspace was tracked in real-time, and the position information and real-time microscopic images were transmitted to the haptic interface side, where the above-described haptic interaction fores were calculated and the haptic control command were sent back to the magnetic tweezer system.

Microrobots (Spherotech SVFM-100-4 ferromagnetic particles, 10.6 μm average diameter) were mixed with deionized water to produce a 1% w/v solution. The solution was then vortexed for 30 seconds and attached to a permanent magnet for magnetization. Environmental objects are non-magnetic glass microparticles (SLGMS-2.527-32 μm diameter, Cospheric LLC) with 1% w/v concentration. The experiment chamber is made from polydimethylsiloxane (PDMS) with a diameter of 3 mm. To decrease the surface friction of microparticles close to the substrate, a 20% w/v concentration of Tween 20 surfactant solution was introduced into the sample medium. 20% w/v NaCl solution was also used for Experiment 1 to mitigate gravitational effect of microrobots.

A. Microrobot Manipulation With Haptic Feedback

The haptic operator was assisted by the haptic feedback to operate microrobots in 3D space. Since the 3D positions of a selected microrobot were synchronized with the haptic probe via artificial stiff spring and damper model, the motion of the selected microrobot was reflected by the operation of the haptic device and vice versa. Experimental demonstration is shown in Fig. 10, in which the microrobot naviagted as controlled in 3D workspace to follow user-controlled trajectories with haptic feedback. Note that the motion of the microrobot on the z-axis followed the haptic control with delay due to the gravity and the viscous conditions of Tween 20 on the surface of the experimental chamber.

B. Dynamic Path Planning With the Path Following Force

When the path planning function was activated, the near-optimal path was displayed on the real-time interface, and path following force was applied to the haptic device. An effective path from the current haptic position to an estimated target was dynamically generated by reflecting the haptic user′s intended haptic operation. Fig. 11 (a) shows the dynamic path generation and microrobot operation by the path following force. In this experiment, the user only held the haptic stylus lightly and let the microrobot reach the target through the dynamic path with the path following force. While the haptic device followed the path by itself, the user could still force the haptic probe to move to the other direction against the path following force to generate a new dynamic path.

C. Micro Object Transportation

The haptic-microrobot system could perform object transportation with haptic assistance in planar space. Since the magnetic force was applied to the global field, all microrobots were actuated by the same directional force. Swarm motion of the multiple microrobots aggregated them together to transport an object with the assistance of the haptic feedback. Fig. 11 (b) shows the operation of the microrobot swarm for object transportation. The haptic device was virtually coupled to the center of mass of the microrobot swarm, while all swarm elements moved in the same direction by the haptic operation due to the global magnetic force field.

VII. Conclusion

A magnetic force-driven microrobot manipulation system with haptic assistance is developed. A large volume data communication strategy is employed to achieve *in situ* real-time teleoperation between two systems in remote locations. The 3D haptic interaction between microrobot and the surrounding environment is implemented by combining ambient and contact forces. To improve the control and tracking accuracy, the effective, near-optimal path is dynamically generated based on the user′s haptic control tendency with the path following force. Eventually, a combination of the attraction force to the selected microrobot, force feedback by the environmental objects, path following force, and real-time visual feedback can improve the navigation performance and path tracking accuracy of the haptic operation for the microrobot controls.

The proposed system is verified with three potential applications in a practical environment by locating two systems in

remote locations, Washington, D.C. and Dallas, Texas, approximately 2138 km apart. For future work, a fully 3D operation will be implemented with a 3D path planning with force feedback. The stability analysis can be conducted using the passivity of the bilateral system with a consideration of the practical time delay. Dynamic path planning can also be improved by learning the arbitrary human user′s haptic operation with deep learning approaches.

Acknowledgment

We thank Louis William Rogowski for proofreading this manuscript.

References

[1] X. Zhang, H. Kim, and M. J. Kim, "Design, implementation, and analysis of a 3-D magnetic tweezer system with high magnetic field gradient," *IEEE Trans. Instrum. Meas.,* vol. 68, no. 3, pp. 680–687, Mar. 2019.

[2] X. Zhang, H. Kim, L. W. Rogowski, S. Sheckman, and M. J. Kim, "Development and implementation of high power hexapole magnetic tweezer system for micromanipulations," in *Proc. IEEE Int. Conf. Robot. Automat.*, 2018, pp. 2670–2675.

[3] E. B. Steager, M. S. Sakar, D. H. Kim, V. Kumar, G. J. Pappas, and M. J. Kim, "Electrokinetic and optical control of bacterial microrobots," *J. Micromechanics Microengineering,* vol. 21, no. 3, 2011, Art. no. 035001.

[4] M. S. Sakar, E. B. Steager, D. H. Kim, M. J. Kim, G. J. Pappas, and V. Kumar, "Single cell manipulation using ferromagnetic composite microtransporters," *Appl. Phys. Lett.,* vol. 96, no. 4, 2010, Art. no. 043705.

[5] S. Fusco, G. Chatzipirpiridis, K. M. Sivaraman, O. Ergeneman, B. J. Nelson, and S. Pané, "Chitosan electrodeposition for microrobotic drug delivery," *Adv. Healthcare Mater.,* vol. 2, no. 7, pp. 1037–1044, 2013.

[6] A. Ferreira, J. Agnus, N. Chaillet, and J.-M. Breguet, "A smart microrobot on chip: Design, identification, and control," *IEEE/ASME Trans. Mechatronics,* vol. 9, no. 3, pp. 508–519, Sep. 2004.

[7] G. Dogangil *et al.*, "Toward targeted retinal drug delivery with wireless magnetic microrobots," in *Proc. IEEE/RSJ Int. Conf. Intell. Robots Syst.*, 2008, pp. 1921–1926.

[8] X. Zhang, L. W. Rogowski, and M. J. Kim, "Closed-loop control using high power hexapole magnetic tweezers for 3D micromanipulation," *J. Bionic Eng.,* vol. 17, no. 1, pp. 113–122, 2020.

[9] J. Tang, L. W. Rogowski, X. Zhang, and M. J. Kim, "Flagellar nanorobot with kinetic behavior investigation and 3D motion," *Nanoscale,* vol. 12, no. 22, pp. 12154–12164, 2020.

[10] X. Zhang, H. Kim, L. W. Rogowski, S. Sheckman, and M. J. Kim, "Novel 3D magnetic tweezer system for microswimmer manipulations," in *Proc. 14th Int. Conf. Ubiquitous Robots Ambient Intell.*, 2017, pp. 382–387.

[11] K. C. Neuman and A. Nagy, "Single-molecule force spectroscopy: Optical tweezers, magnetic tweezers and atomic force microscopy," *Nat. Methods,* vol. 5, no. 6, pp. 491–505, 2008.

[12] U. K. Cheang, M. Dejan, J. Choi, and M. J. Kim, "Towards model-based. Control of achiral microswimmers," in *Proc. ASME Dynamic Syst. Control Conf.*, 2014, Paper no. DSCC2014-6136.

[13] G. D. Wright, J. Arlt, W. C. Poon, and N. D. Read, "Optical tweezer micromanipulation of filamentous fungi," *Fungal Genet. Biol.,* vol. 44, no. 1, pp. 1–13, 2007.

[14] U. K. Cheang, D. Roy, J. H. Lee, and M. J. Kim, "Fabrication and magnetic control of bacteria-inspired robotic microswimmers," *Appl. Phys. Lett.,* vol. 97, no. 21, 2010, Art. no. 213704.

[15] X. Wang *et al.*, "Robotic intracellular manipulation: 3D navigation and measurement inside a single cell," in *Proc. IEEE Int. Conf. Robot. Automat.*, 2018, pp. 2716–2721.

[16] U. K. Cheang, F. Meshkati, D. Kim, M. J. Kim, and H. C. Fu, "Minimal geometric requirements for micropropulsion via magnetic rotation," *Phys. Rev. E,* vol. 90, no. 3, 2014, Art. no. 033007.

[17] Z. Ye, S. Régnier, and M. Sitti, "Rotating magnetic miniature swimming robots with multiple flexible flagella," *IEEE Trans. Robot.,* vol. 30, no. 1, pp. 3–13, Feb. 2014.

[18] F. Long, D. Matsuura, and C.-H. Menq, "Actively controlled hexapole electromagnetic actuating system enabling 3-D force manipulation in aqueous solutions," *IEEE/ASME Trans. Mechatronics,* vol. 21, no. 3, pp. 1540–1551, Jun. 2016.

[19] D. Matsuura, H. Aoki, and Y. Takeda, "Development of a 3D-magnetic tweezer system having magnetic pole positioning mechanism," in *Proc. IEEE Int. Conf. Robot. Automat.*, 2016, pp. 1745–1750.

[20] C. Haber and D. Wirtz, "Magnetic tweezers for DNA micromanipulation," *Rev. Sci. Instruments,* vol. 71, no. 12, pp. 4561–4570, 2000.

[21] M. P. Kummer, J. J. Abbott, B. E. Kratochvil, R. Borer, A. Sengul, and B. J. Nelson, "OctoMag: An electromagnetic system for 5-DOF wireless micromanipulation," *IEEE Trans. Robot.,* vol. 26, no. 6, pp. 1006–1017, Dec. 2010.

[22] Z. Zhang and C.-H. Menq, "Design and modeling of a 3-D magnetic actuator for magnetic microbead manipulation," *IEEE/ASME Trans. Mechatronics,* vol. 16, no. 3, pp. 421–430, Jun. 2011.

[23] F. Amblard, B. Yurke, A. Pargellis, and S. Leibler, "A magnetic manipulator for studying local rheology and micromechanical properties of biological systems," *Rev. Sci. Instruments,* vol. 67, no. 3, pp. 818–827, 1996.

[24] F. Niu *et al.*, "Modeling and development of a magnetically actuated system for micro-particle manipulation," in *Proc. IEEE 14th Int. Conf. Nanotechnol.*, 2014, pp. 127–130.

[25] C. Pacchierotti, L. Meli, F. Chinello, M. Malvezzi, and D. Prattichizzo, "Cutaneous haptic feedback to ensure the stability of robotic teleoperation systems," *Int. J. Robot. Res.,* vol. 34, no. 14, pp. 1773–1787, 2015.

[26] A. M. Okamura, "Methods for haptic feedback in teleoperated robot-assisted surgery," *Ind. Robot: An Int. J.,* vol. 31, no. 6, pp. 499–508, Dec 2004.

[27] C. W. Kennedy, T. Hu, J. P. Desai, A. S. Wechsler, and J. Y. Kresh, "A novel approach to robotic cardiac surgery using haptics and vision," *Cardiovasc. Eng.: An Int. J.,* vol. 2, no. 1, pp. 15–22, 2002.

[28] S. E. Salcudean, S. Ku, and G. Bell, "Performance measurement in scaled teleoperation for microsurgery," in *Proc. CVRMed-MRCAS*, 1997, pp. 789–798, doi: 10.1007/BFb0029304.

[29] A. Kazi, "Operator performance in surgical telemanipulation," *Presence: Teleoperators Virtual Environments,* vol. 10, no. 5, pp. 495–510, 2001, doi: 10.1162/105474601753132678.

[30] A. Pillarisetti, M. Pekarev, A. D. Brooks, and J. P. Desai, "Evaluating the effect of force feedback in cell injection," *IEEE Trans. Automat. Sci. Eng.,* vol. 4, no. 3, pp. 322–331, Jul. 2007.

[31] A. Ghanbari, B. Horan, S. Nahavandi, X. Chen, and W. Wang, "Haptic microrobotic cell injection system," *IEEE Syst. J.,* vol. 8, no. 2, pp. 371–383, Jun. 2012.

[32] C. Pacchierotti, S. Scheggi, D. Prattichizzo, and S. Misra, "Haptic feedback for microrobotics applications: A review," *Front. Robot. AI,* vol. 3, 2016, Art. no. 53.

[33] C. Pacchierotti, V. Magdanz, M. Medina-Sánchez, O. G. Schmidt, D. Prattichizzo, and S. Misra, "Intuitive control of self-propelled microjets with haptic feedback," *J. Micro-bio Robot.,* vol. 10, no. 1-4, pp. 37–53, 2015.

[34] C. Pacchierotti *et al.*, "Steering and control of miniaturized untethered soft magnetic grippers with haptic assistance," *IEEE Trans. Automat. Sci. Eng.,* vol. 15, no. 1, pp. 290–306, Jan. 2017.

[35] A. Bolopion and S. Régnier, "A review of haptic feedback teleoperation systems for micromanipulation and microassembly," *IEEE Trans. Automat. Sci. Eng.,* vol. 10, no. 3, pp. 496–502, Jul. 2013.

[36] M. Asgari, A. Ghanbari, and S. Nahavandi, "3D particle-based cell modelling haptic microrobotic cell injection," in *Proc. 15th Int. Conf. Mechatronics Technol.: Precis. Mechatronics for Adv. Manuf., Service, Med. Sectors*, 2011, pp. 1–6.

[37] S. Faroque, B. Horan, M. Mortimer, and M. Pangestu, "Towards large-scale haptic virtual reality training for micro-robotic cell injection," in *Proc. 5th Int. Conf. Wirel. Netw. Embedded Syst.*, 2016, pp. 1–5.

[38] M. Wu, J. W. Roberts, and M. Buckley, "Three-dimensional fluorescent particle tracking at micron-scale using a single camera," *Experiments Fluids,* vol. 38, no. 4, pp. 461–465, 2005.

[39] M. Wu, J. W. Roberts, S. Kim, D. L. Koch, and M. P. DeLisa, "Collective bacterial dynamics revealed using a three-dimensional population-scale defocused particle tracking technique," *Appl. Environ. Microbiol.,* vol. 72, no. 7, pp. 4987–4994, 2006.

[40] M. A. Oskouie and P. Boulanger, "Using proxy haptic for a pointing task in the virtual world: A usability study," in *Proc. Int. Conf. Augmented Reality, Virtual Reality Comput. Graph.*, 2019, pp. 292–299.

[41] C. H. Park and A. M. Howard, "Real-time haptic rendering and haptic telepresence robotic system for the visually impaired," in *Proc. World Haptics Conf.*, 2013, pp. 229–234.

[42] H. Ding, H. Mitake, and S. Hasegawa, "Continuous collision detection for virtual proxy haptic rendering of deformable triangular mesh models," *IEEE Trans. Haptics,* vol. 12, no. 4, pp. 624–634, Oct.-Dec. 2019.